A Classification of Ice Crystal Habits Using Combined Lidar and Scanning Polarimeter Observations during the SEAC^{4}RS Campaign

NATALIE MIDZAK,[a] JOHN E. YORKS,[b] JIANGLONG ZHANG,[a] BASTIAAN VAN DIEDENHOVEN,[c,d] SARAH WOODS,[e] AND MATTHEW MCGILL[b]

[a] *Department of Atmospheric Sciences, University of North Dakota, Grand Forks, North Dakota*
[b] *NASA Goddard Space Flight Center, Greenbelt, Maryland*
[c] *Columbia University, New York, New York*
[d] *NASA Goddard Institute for Space Studies, New York, New York*
[e] *SPEC, Inc., Boulder, Colorado*

(Manuscript received 9 March 2020, in final form 10 July 2020)

ABSTRACT: Using collocated NASA Cloud Physics Lidar (CPL) and Research Scanning Polarimeter (RSP) data from the Studies of Emissions and Atmospheric Composition, Clouds and Climate Coupling by Regional Surveys (SEAC^{4}RS) campaign, a new observational-based method was developed which uses a *K*-means clustering technique to classify ice crystal habit types into seven categories: column, plates, rosettes, spheroids, and three different type of irregulars. Intercompared with the collocated SPEC, Inc., Cloud Particle Imager (CPI) data, the frequency of the detected ice crystal habits from the proposed method presented in the study agrees within 5% with the CPI-reported values for columns, irregulars, rosettes, and spheroids, with more disagreement for plates. This study suggests that a detailed ice crystal habit retrieval could be applied to combined space-based lidar and polarimeter observations such as *CALIPSO* and POLDER in addition to future missions such as the Aerosols, Clouds, Convection, and Precipitation (A-CCP).

KEYWORDS: Cirrus clouds; Lidars/Lidar observations; Remote sensing

1. Introduction

Cirrus clouds consistently cover almost one-half of Earth's surface and impact the global climate system through their role in the radiative budget (Mace et al. 2009; Wylie and Menzel 1999). Cirrus can either warm or cool the atmosphere depending on the height, particle properties, and optical thickness of the cirrus cloud. While cirrus cloud heights and optical thickness can be measured from space-based remote sensing (Campbell et al. 2015; Holz et al. 2016), cirrus microphysical properties remain a major uncertainty in determining their radiative impacts despite the high frequency of cirrus. Given this uncertainty, studies using radiative forcing models generally assume a random orientation of hexagonal planar or columnar ice crystals, which are only the building blocks to more intricate habits (Fig. 1) (Liou et al. 1983; Baran et al. 2001). This simplified assumption leads to inaccuracies in the estimation of cirrus radiative impacts (Zhang et al. 1999). A main source of ice cloud radiative forcing error stems from scattering parameters of the varying ice crystal habits (Wendisch et al. 2005). A better understanding of cirrus microphysical properties, especially the shape and size of ice crystals, is necessary to more accurately quantify their effects on the climate system.

Ice crystal microphysical properties have long been studied in laboratory and field experiments; however, large-scale in situ measurements are costly and in situ cirrus retrievals are unattainable on a global scale (Bailey and Hallett 2004; Lawson et al. 2019). The option of remote sensing has been explored in the past. For example, van Diedenhoven et al. (2012b, 2013) developed a method for quantifying ice crystals into habit types by utilizing aspect ratio derived from airborne polarimeter observations. However, only broad plate-like or column-like categories can be derived using polarimeter observations alone. Noel et al. (2004) found lidar depolarization ratio to be sensitive to modeled aspect ratio which allowed for a coarse classification of habit types. Still only broad ice crystal categories including plates or spheroids, irregulars and columns were derived from the study. Also, distinguishing small from large ice crystals is a challenging task using lidar observations alone.

As suggested from previous studies (Bailey and Hallett 2009; Noel et al. 2004; van Diedenhoven et al. 2012b, 2016a), to retrieve detailed ice crystal information, combined lidar and polarimeter data, which include aspect ratio, lidar depolarization ratio, asymmetry factor and effective radius are needed. Cloud temperature is also necessary for additional information about the growth regimes of ice crystal habits. Those studies show that plate-like crystals with the lowest aspect ratios (<1) tend to have the highest asymmetry factors (>0.90) and are found at the warmest temperatures of the crystal habits (from $-20°$ to $-40°$C). Compact hexagonal crystals have the next lowest aspect ratio of approximately 1.0 but have depolarization ratios reaching 0.4. Rosettes have the next highest aspect ratio of approximately 2.0 and are found at colder temperatures ($<-40°$C). Because of variations in rosette development and number of branches, rosettes exhibit a range of depolarization ratios (0.25–0.50). Columns tend toward the highest aspect ratios (>3.0) and largest depolarization ratios (>0.50) at cold cloud-top temperatures ($<-40°$C). These findings are of general cirrus ice crystal characteristics; however, in reality, they would vary due to cirrus altitude and temperature,

Corresponding author: Natalie Midzak, natalie.midzak@und.edu

DOI: 10.1175/JTECH-D-20-0037.1

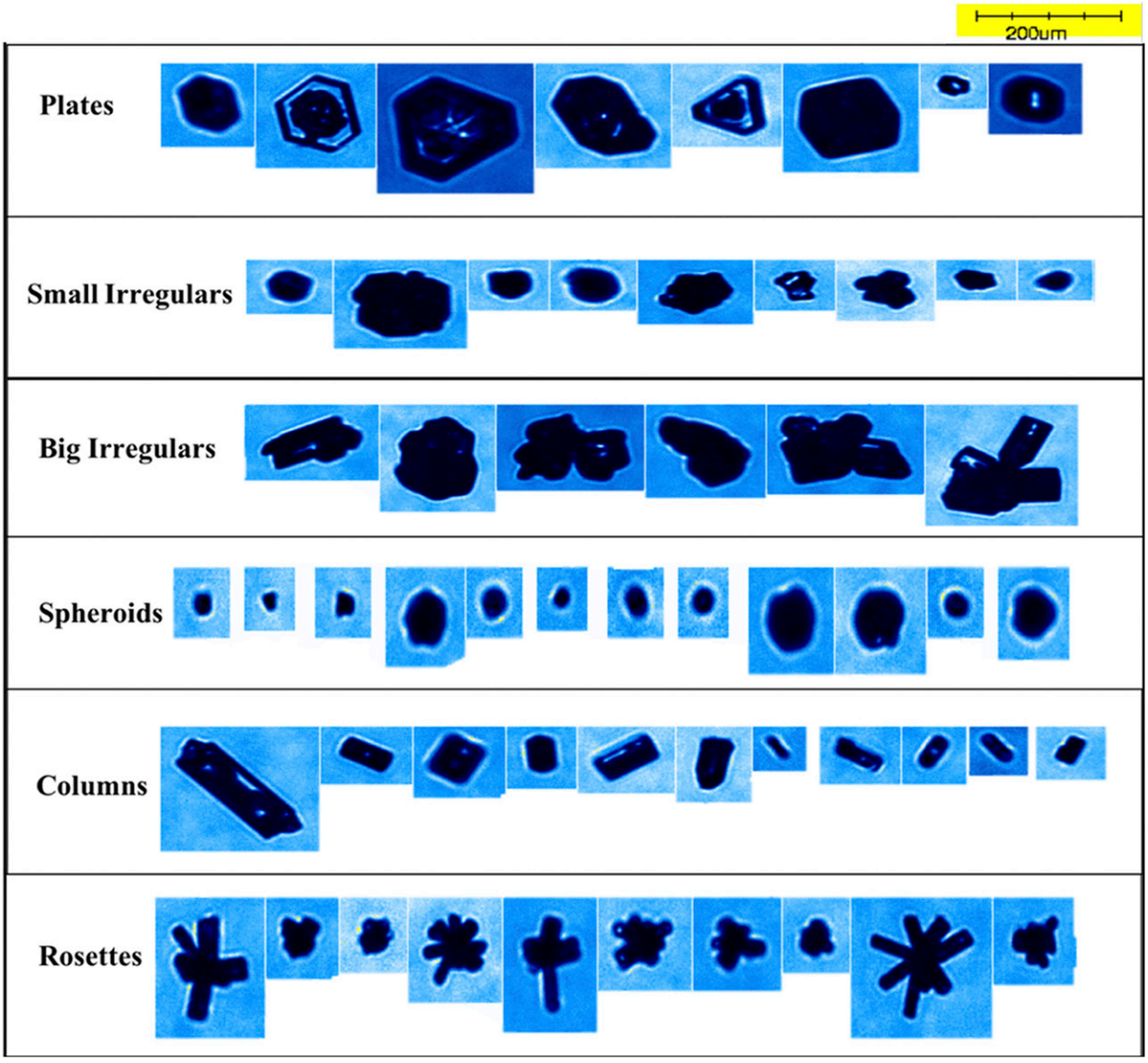

FIG. 1. SPEC CPI imagery collected during an 18 Sep 2013 flight from the SEAC[4]RS field campaign highlighting variations in crystal shape and size for plates, irregulars, spheroids, columns, and rosettes.

along with formation mechanism. Van Diedenhoven (2018) calls attention to joint active lidar and passive multiangle polarimeter as a promising avenue for ice crystal research. To accomplish more detailed habit classifications and gain an understanding of their properties, the combination of retrievals from lidar and polarimeter are necessary.

In this paper, collocated lidar and polarimeter observations of cirrus during the Studies of Emissions and Atmospheric Composition, Clouds and Climate Coupling by Regional Surveys (SEAC[4]RS) campaign collected over the continental United States and Gulf of Mexico are combined and analyzed using a K-means clustering technique. The results of the clustering are classified into columns, plates, rosettes, spheroids and three different type of irregulars. The classification technique is evaluated with in situ data and frequencies of sampled habits from the remote sensing and in situ instruments are presented followed by an uncertainty analysis. This study is the first attempt to determine bulk ice crystal habit types using remote sensing data with the detail typical of in situ sensors. The ice particle habit results presented in this paper strengthen our understanding of cirrus cloud scattering parameters, while the classification method shown here can be used on other airborne remote sensing datasets and future space-based datasets to improve parameterizations of ice crystal habits and calculations of cirrus radiative forcing.

2. Data

In this study, spatially and temporally collocated NASA Cloud Physics Lidar (CPL) and Research Scanning Polarimeter

(RSP) data from the SEAC^{4}RS campaign were used for the study period of August–September 2013. The derived ice crystal habit types from the study were also intercompared with the SPEC, Inc., Cloud Particle Imager (CPI) data.

a. CPL

NASA's CPL is an elastic backscatter lidar providing multiwavelength backscatter measurements of clouds and aerosols at 1064, 532, and 355 nm (McGill et al. 2002). Depolarization ratio, used to discriminate between liquid and ice clouds, is measured using the 1064 nm channel while cloud optical properties (i.e., extinction coefficient, ice water content) are retrieved from the 1064- and 532-nm channels (McGill et al. 2003). CPL has participated in over two dozen field campaigns since its first deployment in 2000 and serves as a reliable tool in the study of atmospheric profiling at high spatial and temporal resolutions. CPL raw data have a temporal resolution of 10 Hz and vertical resolution fixed at 30 m. The data are averaged to 1 s when creating data products, which equates to a 200 m horizontal resolution for an aircraft speed of 200 m s^{-1}. When mounted aboard NASA's ER-2 aircraft CPL points off-nadir by 2° because of the pitch of the aircraft. Therefore, the effect of horizontally oriented ice crystals on CPL data is negligible (Yorks et al. 2011).

Once instrument corrections and calibration are applied to raw photon counts, CPL provides profiles of total attenuated backscatter (ATB) and the ratio of perpendicular to parallel backscatter (depolarization ratio) of clouds and aerosols (McGill et al. 2007). CPL produces linearly polarized light, and measures the perpendicular and parallel planes of polarization of the backscattered light using a beam splitter in the receiver optics. The linear volume depolarization ratio is the ratio of the perpendicular polarized 1064-nm attenuated backscatter coefficient to the parallel polarized 1064-nm attenuated backscatter coefficient. Deriving accurate depolarization ratios requires knowledge of the depolarization gain ratio, which describes the relative gain between the perpendicular and parallel channels. Yorks et al. (2011) reports that the error in gain ratio is less than 3%. Level 2 algorithms use ATB profiles and depolarization ratio to further derive cirrus physical and optical properties. CPL level 2 algorithms categorize identified layers as ice clouds, liquid water clouds, or eight different aerosol types. A cloud phase (CP) algorithm is used to discriminate between liquid water clouds and ice clouds. High confidence ice clouds have a midlayer temperature less than −20°C and a depolarization ratio greater than 0.25 (Yorks et al. 2011). Temperatures provided from MERRA-2 are interpolated to the CPL data and reported in the layer temperature product.

Five years of cloud optical properties from CPL were analyzed extensively by Yorks et al. (2011). A strong dependence of increasing layer volume depolarization ratio with decreasing temperature was found for all cirrus clouds. Statistics of ice cloud volume depolarization ratios and temperatures were explored to determine thresholds for cloud phase discrimination which are applied in this study. Previous research has also examined the sensitivity of lidar depolarization ratio to aspect ratio for modeled randomly oriented hexagonal ice crystals. Results show that depolarization ratio can be used to classify ice crystals into three categories: thin plates or spheroids, big and small irregulars and columns. Uncertainties due to depolarization variability are lowest for columns (less than 4%) and generally less than the maximum of 15% for other habits (Noel et al. 2004). However, lidar alone does not provide sufficient information for a more detailed classification.

b. RSP

The RSP is a multichannel, multiangle airborne polarimeter with nine spectral channels in visible/near-infrared and shortwave infrared bands providing measurements of total reflectance and polarized reflectance derived from the I, Q, and U components of the Stokes vector. RSP scans along track over an ~120° angular range utilizing the fields of view of six boresighted refractive telescopes, which contribute to its 14-mrad field of view (similar to that of CPL). Each pixel is sampled at 152 viewing angles and 0.8° intervals (Cairns et al. 2003). When on board the NASA ER-2, the RSP's viewing angles drop to 134 usable angles (Sinclair et al. 2017). RSP derives the cloud-top height using a multiangle parallax method (Sinclair et al. 2017). Subsequently, RSP data are mapped so that multiangle views are available as a function of location at cloud top (Alexandrov et al. 2012). For RSP mounted on the ER-2, it takes about 2–3 min to collect all viewing angles for a location on a cirrus cloud top. Ice-topped clouds are selected by means of a liquid index derived from multiangle polarimetry measurements around the 140° scattering angle, where liquid-topped clouds lead to a pronounced cloudbow feature (van Diedenhoven et al. 2012b). Clouds identified by RSP with a liquid index less than 0.3 and a cloud optical thickness greater than 5 are considered to be ice. The 1.59- and 2.25-μm channels are utilized in ice cloud retrievals for their sensitivity to ice/water discrimination (van Diedenhoven et al. 2012a).

RSP employs the first remote sensing method of retrieving ice crystal asymmetry factor from multidirectional polarized measurements of aspect ratio and crystal distortion (van Diedenhoven et al. 2012a, 2013). RSP retrievals rely on individual hexagonal columns and plates to serve as proxies for more complex habit types (van Diedenhoven et al. 2013). The asymmetry factor values are determined by a closest fit to measured multidirectional polarized measurements from a lookup table consisting of randomly oriented hexagonal columns and plates with nearly continuous values of aspect ratio and crystal distortion levels (van Diedenhoven et al. 2012b). The distortion parameter (Macke et al. 1996) is a proxy for randomization of the crystal shape caused by a number of factors, such as large-scale crystal distortion and complexity, microscale surface roughness, and impurities within the crystals (Hong and Minnis 2015; Liu et al. 2014; Neshyba et al. 2013). A definition of aspect ratio with an upper limit of unity for both columns and plates is used in this study (van Diedenhoven et al. 2016a). Here aspect ratio is the ratio between dimensions of components of ice crystals. Given this definition, ice crystals must be specified as column-like or plate-like, as is standard for RSP ice cloud products. Once the crystal type is known the inverse of aspect ratio can be used to separate column-like crystals from their plate-like counterparts.

Despite this separation, a finer habit classification is necessary for accurate representation of ice crystal shapes. Additionally, effective radius is retrieved at 1.59 and 2.25 μm, utilizing the 2.25-μm channel in this study for its ability to penetrate deeper into ice clouds (van Diedenhoven et al. 2016b). RSP effective radius is ¾ of the average ice volume divided by the average projected area (van Diedenhoven et al. 2016b). A lookup table approach is used for effective radius retrievals that is described by van Diedenhoven et al. (2014, 2016a). Note that, for each observation, an ice optical model is used for the effective radius retrievals that is consistent with the retrieved asymmetry factor for that observation, as described by van Diedenhoven et al. (2014).

c. CPI

The SPEC, Inc., CPI records high-resolution (2.3-μm pixel) digital images of individual ice cloud particles that pass through the sample volume of the imager (Lawson et al. 2001). Within each frame, CPI can record upward of 25 particles simultaneously. The collected images are processed using SPEC, Inc., software which derives crystal length, width, area and perimeter (Baker and Lawson 2006). These descriptors are then used to classify the ice crystals into seven habits: spheroid, column, plate, rosette, budding rosette, small irregular, and big irregular. A complete description of CPI classification criteria can be found in the appendix of Lawson et al. (2006a).

d. SEAC^{4}RS

Data from these instruments were collected during the NASA SEAC^{4}RS campaign. SEAC^{4}RS took place in August and September 2013 and was based outside Houston, Texas (Toon et al. 2016). During the campaign, 57 science flights were completed by NASA's ER-2 and DC-8 along with the SPEC, Inc., Learjet spanning the continental United States and the Gulf of Mexico. A large suite of remote sensing and in situ instrumentation was implemented to study radiation, chemistry, and cloud microphysics. The CPL and RSP were both on board NASA's ER-2 for these flights, flying at a nominal altitude of 18–20 km (Sinclair et al. 2017). The following analysis consists of data from 10 flights over the course of the campaign: 2, 6, 21, 27, and 30 August and 4, 11, 13, 18, and 23 September. Continental and maritime cirrus were sampled during these flights, with special attention on the 18 September flight in which all three aircraft flew though a region of maritime convection (Toon et al. 2016).

3. Method

a. Ice crystal habit definitions

The habit descriptions used in this study follow those put forth by Bailey and Hallett (2002, 2004, 2009) and Lawson et al. (2006a), as also shown in Fig. 1 using CPI imagery data collected on 18 September 2013 during the SEAC^{4}RS campaign. Here "plates" describes hexagons with a face width larger than height which results in an aspect ratio below unity. This category of crystals includes thick and thin plates along with asymmetric irregular plate-like crystals and is therefore not limited to pristine, symmetrical plates. "Columns" are hexagonal with a length greater than their face width resulting in aspect ratios greater than 1. Columns can be solid or hollow and short or long. Recent literature such as Bailey and Hallett (2009) documents that an overemphasis of symmetric crystal habits exists in literature. The idealized shapes once found in habit diagrams are quite rare and the reality of defective and irregular crystals must be acknowledged (Bentley and Humphreys 1931; Bailey and Hallett 2009). "Spheroids" are particles greater than 50 μm in diameter and appear spherical unless studied under close magnification. These are quasi-spherical compacted particles usually highly faceted and distorted. "Rosettes" presented in this study include budding rosettes which are not fully developed and general rosette-shaped particles which have multiple columnar structures gathered at a central point. "Irregulars" are composed of compact faceted crystals that account for nonsymmetric and defective crystals that do not fit into any of the above categories. Irregulars with aspect ratios less than 1 are categorized as plate-like irregulars, which consists of a larger and smaller category, while those with aspect ratios larger than 1 are column-like irregulars which likely contain side planes.

b. Combined CPL–RSP cirrus retrievals

Two of the most promising instruments for ice crystal retrievals are active lidar and passive multiangle polarimeters (van Diedenhoven 2018). Lidar's unique advantage to obtain vertical profiles of clouds allows for more detailed structure than passive or in situ sensors can provide on one overpass. Additionally, the sensitivity of lidar to optically thin layers allows for detections unattainable by cloud radars (Comstock et al. 2002). Multidirectional polarized measurements of varying ice crystal shapes provide information on the phase function and scattering of light by crystals using a minimum of three simultaneous observations. Thus, using collocated CPL and RSP data, a new method was developed for classifying ice crystal habit types from retrieved CPL–RSP observations in this study.

1) CPL–RSP COLLOCATION

Coincident CPL and RSP observations were identified from the flights previously listed. These data were collocated temporally by synchronizing the time of overpasses for observations with the closest time stamps between the CPL curtains and RSP's near-nadir views. The maximum time allowed between observations to be considered collocated was one minute. CPL and RSP were both mounted on the ER-2 and have similar fields of view so observations could be readily intercompared. Despite these similarities, CPL and RSP have different sensitivities to cirrus clouds. For RSP cloud optical thickness greater than 5, the polarized reflectance does not depend on the optical thickness (Chepfer et al. 2001). However, for optical thicknesses less than 5 the cloud apparent optical thickness must be included in the lookup table used for determining asymmetry factor. The apparent optical thickness is determined by minimizing the difference between simulated and total reflectance (van Diedenhoven et al. 2012b). One of the advantages of including CPL for this study is its unique

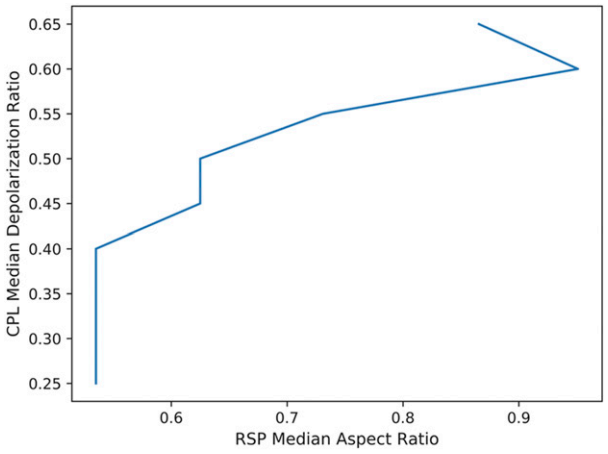

FIG. 2. Evolution of depolarization ratio with aspect ratio for collocated lidar–polarimeter data obtained during the SEAC^{4}RS campaign.

ability to measure optically thin cirrus layers (COD $<$ 0.03) with high accuracy (McGill et al. 2002). CPL can also measure the vertical structure of cirrus which is not possible for CPI or passive sensors.

A ray-tracing simulation of light polarization as it interacts with hexagonal-based ice crystals is compared with retrieved CPL depolarization ratios of randomly oriented ice crystals in Noel et al. (2004). The depolarization ratio was found to be sensitive to the modeled aspect ratio which allowed for a coarse classification of ice crystals into three groups (and four habits) consisting of plates or spheroids with the lowest depolarization and aspect ratios, irregulars, and columnar crystals which are highly depolarizing and have larger aspect ratios. This comparison was recreated using CPL and RSP observations obtained during SEAC^{4}RS (see Fig. 2) to observe the evolution of linear depolarization ratio with aspect ratio. Two definitions of aspect ratio are commonly used. If AR = L/W, where L is the prism length and W is the crystal basal plane width, the resulting aspect ratio is greater than 1 for columns and less than 1 for plates. Van Diedenhoven et al. (2016a) propose a definition of aspect ratio as AR = min(L, W)/max(L, W) that limits the aspect ratio to below unity for both plates and columns. In using this definition, it needs to be specified whether crystals are plate-like or column-like. Figure 2 does not distinguish between plate-like or column-like crystals, therefore the definition of aspect ratio is below unity for all crystal habits using the definition of aspect ratio set forth by van Diedenhoven et al. (2016a). To the authors' knowledge, this is the first confirmation that data from observations matches modeled data of the evolution of depolarization ratio with increasing aspect ratio. Figure 2 demonstrates the relationship between depolarization ratio and aspect ratio; therefore it validates the use of combined lidar and polarimeter data to classify ice crystal habits.

The CPL properties investigated in this study are layer-integrated parameters, as such the results presented are bulk cloud-top volume measurements of coincident lidar and polarimeter data. These bulk retrievals represent data on an ~1 km vertical by ~250 m horizontal "box." Conversely, the CPI records individual ice crystals that are detected and trigger the pulse of the imaging laser (Lawson et al. 2001). Therefore, it is assumed that the bulk volume measurements presented in this study are representative of the individual cirrus particle properties.

2) K-MEANS BASED CLUSTERING ANALYSIS OF ICE CRYSTAL HABIT TYPES

Approximately 2000 ice crystal observations were identified in the collocated flight segments. Each observation made by CPL was additionally filtered to ensure that only ice clouds were being analyzed. Only cloud layers classified as cirrus by a CP value of 3 were used. Additionally, these layers had to be colder than −20°C and have a depolarization ratio greater than 0.25. Because of the passive nature of RSP, only cloud-top properties are retrieved and used in this study. Additionally, CPL signal attenuates before reaching cloud base for optically thick clouds. Therefore, results presented are for cloud tops of optically thick cirrus (COD $>$ 3.0). Once high confidence ice clouds classified from CPL and RSP were collocated and filtered, K-means clustering analysis was used to group ice crystals by the following features: depolarization ratio (CPL), aspect ratio (RSP), asymmetry factor (RSP), effective radius (RSP), and cloud-top temperature (CPL). RSP's crystal distortion retrievals were not used for clustering, since, for most cases, the maximum distortion level of 0.7 was retrieved during SEAC^{4}RS. The tendency to retrieve maximum distortion is consistent with previous findings using POLDER data (Hioki et al. 2016). However, we do report on statistics of distortion values for the different clusters. Seven initial cluster centers were selected to represent the habits identified by CPI. To distinguish between planar and columnar crystals, initial clusters were separated based on aspect ratio. Clusters were assigned to data points with aspect ratios less than 1, which encompassed plates, plate-like irregulars, and spheroids. Next, clusters were assigned to data points with aspect ratios greater than 1, which were made up of columns, column-like irregulars, and rosettes. The data were normalized to allow all observations to be compared regardless of their units and to allow for an equal weighting of observations during the clustering. Through the iterative process each point in the normalized features was assigned to its closest cluster center and the seven cluster centers were updated to be the mean of the points within the cluster. The process terminates when the algorithm converges and there are no changes in cluster assignments within a threshold. Clustering was done for all SEAC^{4}RS cirrus observations and for the 18 September 2013 case study.

The K-means method was chosen for its efficiency in clustering several variables with many data points into a small number of K known values. Using the Euclidean mean produces tighter cluster centers than some other distance metrics (Singh et al. 2013). Additionally, data points are able to change cluster assignments as centroids are computed iteratively (Gan et al. 2007). Relative tolerance with regard to iteration of 1×10^{-4} was set to declare convergence. The K-means approach resulted in the classification of ice crystal habits into distinct

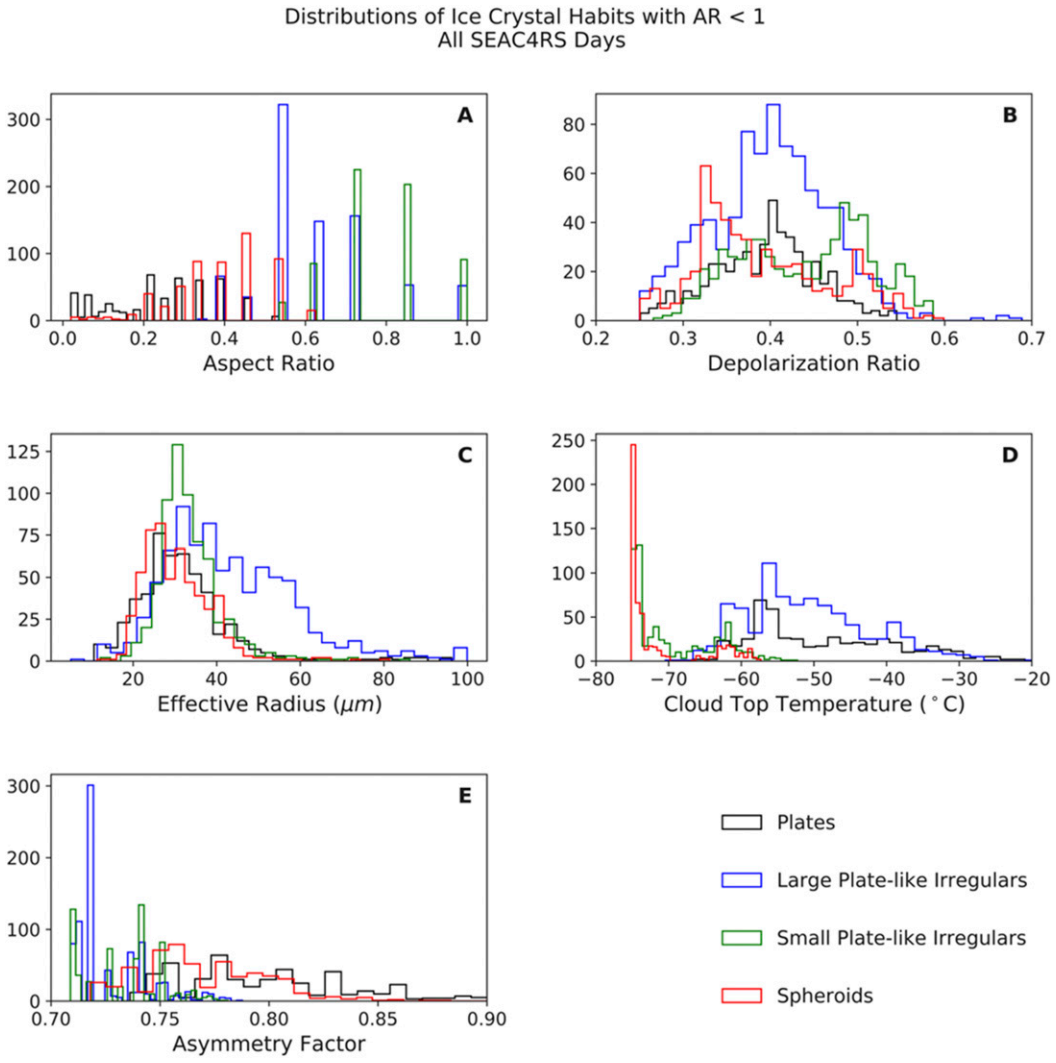

FIG. 3. Distributions of collocated observations of plate-like ice crystal habits for (a) aspect ratio, (b) depolarization ratio, (c) effective radius, (d) cloud-top temperature, and (e) asymmetry factor for all SEAC^{4}RS data.

clusters utilizing combined CPL and RSP observations for the first time.

4. Results

The results of *K*-means clustering for each of the features listed above are presented in Figs. 3 and 4 for the entire SEAC^{4}RS dataset. Two sets of clusters are presented: those for aspect ratios less than or greater than 1.0 (Figs. 3, 4, respectively). The clusters were assigned ice crystal habits based on their defining characteristics (corresponding statistics for the clusters are summarized in Table 2).

Plates were categorized as the cluster with the lowest mean aspect ratio (0.24) and highest mean asymmetry factor (0.80). These are typical characteristics of plates and have been previously reported (see Table 1). As previously noted, the definition of plates is not limited to symmetric, ideal hexagonal plates. In this study, the plate category includes thick, thin and asymmetric polycrystalline plate-like crystals; samples of which are shown in Fig. 1. Thin plates have the highest asymmetry factors with values surpassing 0.9, whereas thicker plates or aggregates of plates tend toward lower values of 0.73. Plates also have relatively warm cloud-top temperatures within this dataset, with a mean cloud-top temperature of −48°C. It is expected that plates have warmer temperatures than columnar crystals based on previous findings summarized in Table 1.

At the very coldest temperatures, with a mean value of −71°C, small compact particles are found. At these temperatures it is likely that the particles are barely developed budding rosettes, small columnar crystals and irregular polycrystals (Bailey and Hallett 2009). This cluster is classified as spheroids; however, it should not be assumed that the particles are spheres but rather that they are distorted, spherical crystals that may be still developing into a distinct habit.

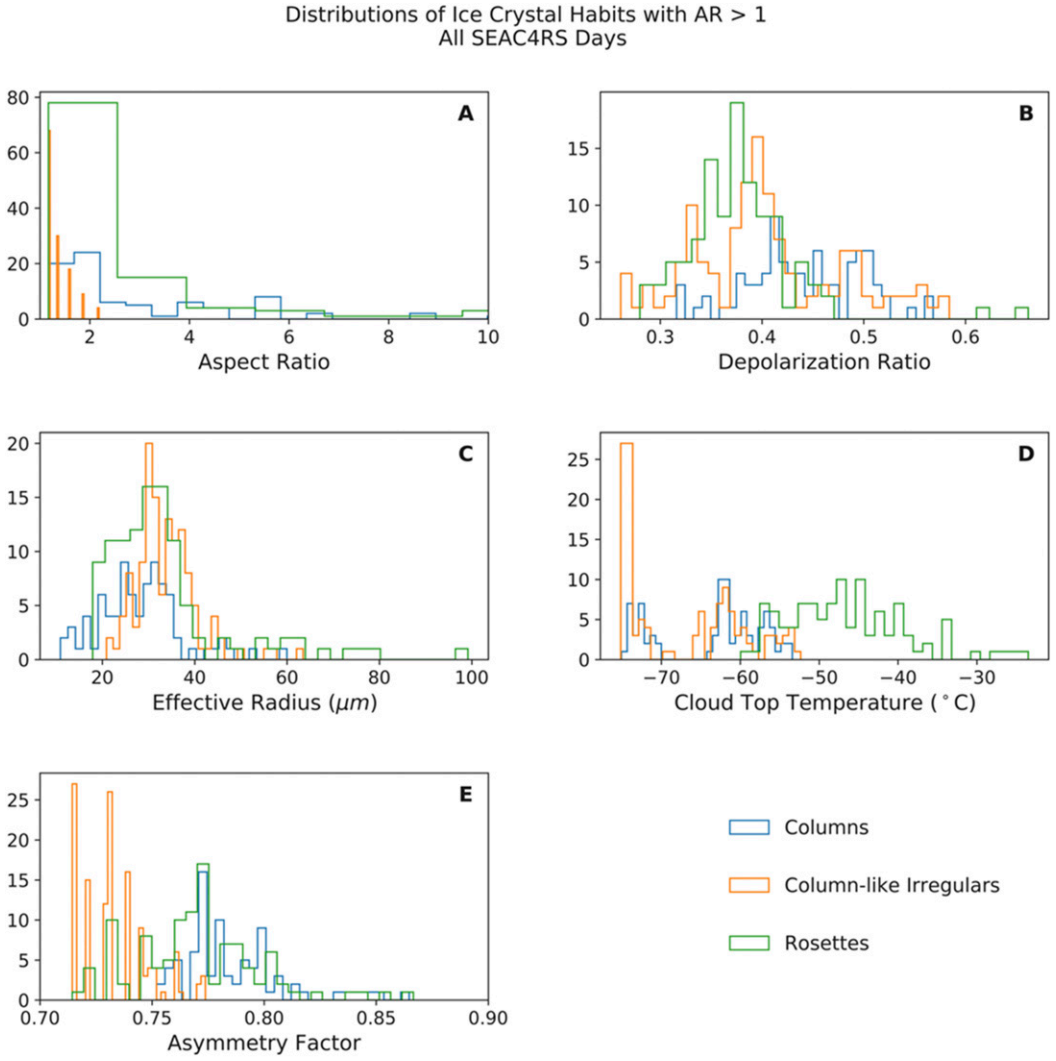

FIG. 4. As in Fig. 3, but for column-like ice crystal habits.

The remaining clusters with aspect ratios less than unity are classified as irregulars within the plate-like regime. Irregulars within this regime were separated into two groups to further differentiate habits based on size: large and small plate-like irregulars. The first group of irregulars have a mean aspect ratio of 0.62. This group is warmer (mean temperature of −50°C) and larger (mean radius of 43 μm) than the second cluster of irregulars. The colder and smaller group of irregulars with a mean cloud-top temperature of −69°C and effective radius of 33 μm, has a higher aspect ratio of 0.78 resulting from a larger deviation from symmetry than the first group of irregulars. Both irregular clusters have asymmetry factors of approximately 0.73 suggesting dense crystals or distorted aggregates of crystals. High mean depolarization ratios of 0.40 and 0.44, respectively, confirm the irregular nature of these clusters. Irregulars also have the largest effective radii of

TABLE 1. Previously published values of aspect ratio, asymmetry factor, cloud temperature, and depolarization ratio of various crystal habits.

	Compact hexagonal	Long columns	Plates	Rosettes
Aspect ratio (van Diedenhoven et al. 2012b, 2016)	~1.0	>3.0	0.01 to 1.0	>2.0
Asymmetry factor (van Diedenhoven et al. 2012b, 2016)	0.70–0.80	0.80–0.90	0.90–0.95	0.80–0.90
Temperature (Bailey and Hallett 2009)	From −20° to −70°C	From −40° to −60°C	From −20° to −40°C	From −40° to −60°C
Depolarization ratio (Noel et al. 2004)	<0.40	>0.50	<0.25	0.25 to 0.50

TABLE 2. Summary of CPL and RSP ice crystal habit statistics for the entire collocated SEAC^{4}RS dataset.

	Plates	Large plate-like irregulars	Small plate-like irregulars	Spheroids	Columns	Column-like irregulars	Rosettes
Samples	495	834	631	556	83	129	108
Mean aspect ratio	0.238	0.621	0.787	0.383	3.63	1.35	2.93
Median aspect ratio	0.245	0.535	0.731	0.391	2.18	1.17	1.870
Std dev aspect ratio	0.131	0.152	0.124	0.124	3.31	0.259	4.53
Mean depolarization ratio	0.394	0.400	0.440	0.392	0.441	0.404	0.377
Median depolarization ratio	0.399	0.402	0.447	0.373	0.438	0.395	0.374
Std dev depolarization ratio	0.059	0.067	0.073	0.075	0.056	0.074	0.054
Mean effective radius	31.86	43.21	33.47	30.57	28.03	33.83	33.54
Median effective radius	29.85	40.16	32.04	29.11	28.04	33.00	30.60
Std dev effective radius	12.15	15.64	7.67	8.31	9.04	6.54	14.18
Mean cloud-top temperature	−48.77	−50.72	−69.32	−71.42	−63.47	−67.41	−46.36
Median cloud-top temperature	−51.70	−51.69	−71.85	−74.30	−61.95	−71.65	−47.05
Std dev cloud-top temperature	10.05	8.64	5.78	5.38	6.55	7.39	7.61
Mean asymmetry factor	0.800	0.727	0.733	0.769	0.786	0.733	0.769
Median asymmetry factor	0.793	0.718	0.740	0.767	0.781	0.731	0.768
Std dev asymmetry factor	0.043	0.016	0.017	0.029	0.023	0.015	0.028
Mean distortion	0.577	0.659	0.616	0.586	0.558	0.656	0.589
Median distortion	0.700	0.700	0.600	0.650	0.600	0.700	0.600
Std dev distortion	0.199	0.075	0.079	0.148	0.023	0.062	0.098

clusters analyzed with aspect ratios less than unity with mean values of 43 and 33 μm. Although distortion parameter was not part of the clustering procedure, there was a distinct difference in the distortion values of irregulars and plates or columns. The average distortion parameter of the irregulars is greater than that of plates, which is consistent with greater crystal complexity for irregulars than for plates. A large cloud-top temperature difference exists between the two irregular clusters. The smaller irregular cluster has minimum temperatures reaching −75°C while the larger irregular cluster has minimum temperatures nearly 15°C warmer. These temperature differences suggest the second cluster contains more compact crystals while those in the first group are thin. This is confirmed by the peak in lower asymmetry factors for the second group of irregulars (e.g., Table 2).

Distributions of ice crystal habits with aspect ratios greater than 1.0 for SEAC^{4}RS are shown in Fig. 4. Rosettes and columns typically have aspect ratios greater than unity and can exceed aspect ratios of 4 (Bailey and Hallett 2009). In this dataset, the cluster with largest mean aspect ratios (2.63) and highest mean depolarization ratio (0.44) was identified as columns. These values agree with those listed in Table 1 which were found in previous studies. Additionally, column temperatures fit well within the known column temperature regime which is colder than −40°C. Overall temperatures for the dataset are colder than previously published findings (Table 1). This is due to the high altitude at which cloud-top temperatures are retrieved as opposed to lower altitude in situ measurements. Columns with mean temperatures of −63°C suggest that they are found near cloud top where in situ measurements are difficult to obtain. Rosettes also have high aspect ratios with values increasing as the number of attached branches increases (Um et al. 2015). Therefore, the group with the second highest mean aspect ratio (2.93) is categorized as rosettes. An example of the utility of combined retrievals can be highlighted on inspection of plates and rosettes. The mean depolarization ratios are quite similar for plates and rosettes (0.394 versus 0.377). However, the aspect ratio for the habits is very different (0.238 vs 2.93). Classification of these habits into distinct types is possible only though the combination of sensors.

The associated standard deviation of rosettes is large due to the varying stages of development of the crystals and their branches. Rosettes fall within the expected temperature range (from −30° to −40°C) reported by Bailey and Hallett (2009). Those found in warmer regions transition to grow in width and can contain side planes or hollow branches, while rosettes found in the colder temperatures have more distinct branches intersecting the central core. At the lowest temperatures where rosettes are found (<−50°C), there is a retardation in bullet growth and crystals are small and compact. These temperatures match those found by Lawson et al. (2010) for results in cirrus. Rosette depolarization ratios are lower than for columns (0.37 vs 0.44) as is expected based on values of depolarization ratio reported by Noel et al. (2004).

The final cluster of crystals are identified as column-like irregulars. Although they are within the column regime, the mean aspect ratio of this group (1.35) is lower than that of columns or rosettes. The mean asymmetry factor (0.73) is also lower than that of other habits with aspect ratios greater than one. As also seen for the plate-like regime, the average distortion parameter of the column-like irregulars is greater than that of columns, consistent with their greater complexity.

The frequency of each assigned habit classification for the collocated CPL–RSP data during all of the SEAC^{4}RS

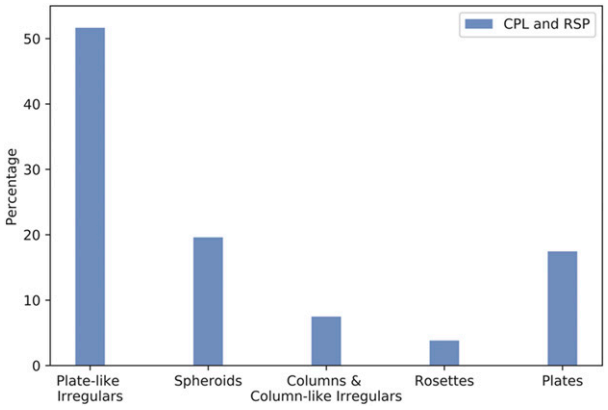

FIG. 5. Frequencies of ice crystal habits for all collocated SEAC^{4}RS data dominated by plate-like irregulars (52.21%), followed by spheroids (20.50%), plates (16.08%), columns and column-like irregulars (7.51%), and rosettes (3.70%).

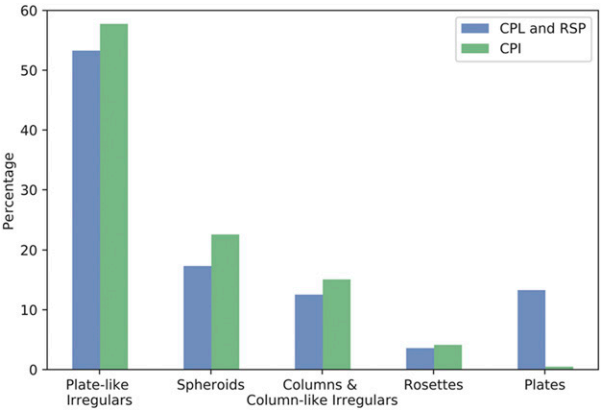

FIG. 6. Frequencies of ice crystal habits classified by SPEC CPI (green) and the newly developed CPL–RSP technique (blue) for a case study on 18 Sep 2013 from the SEAC^{4}RS campaign. Agreement for irregulars, spheroids, columns, and rosettes is within 5%, with less agreement for plates (~16%).

campaign are presented in Fig. 5. Irregulars with low aspect ratios dominate the dataset with a frequency of 52.21% followed by spheroids (20.50%), plates (16.08%), columns and column-like irregulars (7.51%), and rosettes (3.70%). These results compare favorably to those previously found by Noel et al. (2004) in which CPL and CPI data were analyzed from the CRYSTAL-FACE field campaign. The habits found in convective anvils sampled by Noel et al. (2004) were dominated by irregulars (~60%), followed by plates and spheroids (34%) and columns (6%). Crystals could only be categorized into broad groups composed of plates/spheroids, irregulars, and columns based on depolarization and aspect ratio. Because lidar depolarization ratio is not a function of particle size or particle asymmetry, no distinctions could be made between large and small crystals or rosettes and columns which both have aspect ratios greater than unity. Most of the SEAC^{4}RS data sampled tropical anvil cirrus over the Gulf of Mexico, with 75% of data falling in latitudes between 19.11° and 27.56°N and longitudes between 124.2° and 92.4°W. The findings presented also compare favorably to those of Lawson et al. (2010) in which tropical anvil cirrus were sampled. Lawson et al. (2010) reported that fresh anvils rarely contain rosettes, but instead were composed mostly of irregulars. These results highlight the agreement in current and previous findings and showcase the utility of a combined remote sensing retrieval technique for ice crystal classifications.

5. Validation and uncertainty

The previously described analysis was applied to the case study date of 18 September 2013 to classify ice crystals sampled in anvil cirrus into habit types. SPEC CPI habit classifications were compared with classifications made using the combined CPL and RSP retrieval method. This is the only flight day of nearly coincident CPL, RSP, and CPI observations from the SEAC^{4}RS campaign.

The results of this comparison are shown in Fig. 6. In both cases irregulars with low aspect ratios composed over half of all observations. Also, comparisons for both retrieval methods agree within 5% in frequency for plate-like irregulars, spheroids, columns and column-like irregulars and rosettes. The least observed habit for the combined retrieval technique was rosettes; however, the least observed habit from CPI was plates which composed only 0.4% of observations. A source of the disagreement stems from differences in habit classification definitions. In a study conducted by Lawson et al. (2006b) habits classified automatically by the CPI software were manually inspected to estimate the accuracy of the automatic classification. It was found that 12% of habits were misclassified with plates accounting for the largest percentage of misclassifications (27%). The definition of plates in this study does not limit crystals only to symmetric plates so this category likely includes irregulars. Sampling differences also contribute to the disagreement. While CPI captures individual particles, CPL and RSP sample bulk cloud properties. Additionally, the measurements from CPL–RSP and CPI are not exactly coincident. Both CPL and RSP were mounted on board the ER-2 while CPI was on the Learjet. These two aircraft never flew in a stacked alignment with the ER-2 above the Learjet, but rather sampled the same clouds at slightly different times. For the first half of this flight segment the Learjet flew at a lower altitude than the ER-2. While the CPI initially flew just above 6 km, the CPL cloud layer was between 10 and 12 km. This means the CPI on board the Learjet was sampling lower altitude, warmer clouds than CPL. This altitude difference can explain the higher frequency observations of plate-like irregulars and spheroids made by CPI. For the latter half of this segment the Learjet sampled clouds at the same altitude as the ER-2. Cloud tops were between 12 and 13 km indicating cold clouds likely composed of columns and rosettes. Thus, the comparison is not "apples to apples" throughout the flight, but we assume that there is little cloud evolution over the minutes of sampling difference so that the CPI data are representative of the bulk cloud-top retrievals by the lidar and polarimeter. To the authors' knowledge, there are no existing datasets that include

TABLE 3. Weights of individual attributes used to calculate overall uncertainty in each habit type.

	Aspect ratio	Depolarization ratio	Cloud-top temperature	Asymmetry factor	Effective radius
Plates	0.08	0.045	0.47	0.35	0.049
Large plate-like irregulars	0.34	0.03	0.23	0.26	0.11
Small plate-like irregulars	0.23	0.05	0.28	0.21	0.22
Spheroids	0.43	0.06	0.25	0.17	0.08
Columns	0.07	0.13	0.30	0.40	0.02
Column-like irregulars	0.1	0.02	0.10	0.50	0.27
Rosettes	0.10	0.20	0.30	0.13	0.21

exactly coincident lidar, polarimeter, and cloud probe imagery to complete a more apples-to-apples study.

For all cirrus layers on 18 September 2013, the mean CPL penetration depth is 1.66 km. Van Diedenhoven et al. (2014) estimated that effective radius RSP retrievals can be assumed to pertain to the top 1 km of the cloud based on all the data collected during the SEAC^{4}RS campaign utilizing the 2.25-μm channel. Depolarization ratio varies by 0.07 throughout the entire CPL penetration depth on 18 September 2013 and only varies by 0.04 in the lowest 0.66 km of the cirrus layer. Therefore, the layer-integrated depolarization ratio is representative of the mean depolarization ratio within the layer, which in turn is representative of the cloud-top properties for the optically thick cirrus clouds included in this study.

To quantify the uncertainty in the presented analysis, the importance of each attribute used in the classification was assessed. To do this, the *K*-means technique was repeated five times, each time removing one of the following parameters: aspect ratio, depolarization ratio, cloud-top temperature, asymmetry factor, and effective radius. The resulting clusters were classified into seven habits, just as before. The frequencies of habit types were compared to the frequencies when all five attributes were present in the analysis. Differences in frequencies were attributed to the parameter that was eliminated in that particular trial. For each habit, the differences in frequencies due to removing an attribute were summed. The change in frequency due to each attribute was divided by the sum and this fractional difference was used as the weight. Table 3 summarizes the weights for each attribute used in the habit classification. Whichever missing parameter caused the largest change in frequency was deemed the most important. This analysis provided weights which could be applied to the corresponding attributes.

Once an appropriate weight was established for each parameter in the classification, the uncertainty of a cluster from each attribute is computed by dividing the normalized variance in each attribute for a cluster by the normalized values of that attribute, then multiplied with the corresponding weight as defined in Table 3. The overall uncertainty for a cluster is thus computed by summing computed uncertainties from all used attributes for that cluster, as suggested in Eq. (1):

$$\Delta c = \frac{\partial c}{\partial T}\Delta T + \frac{\partial c}{\partial \mathrm{dp}}\Delta \mathrm{dp} + \frac{\partial c}{\partial \mathrm{AR}}\Delta \mathrm{AR} + \frac{\partial c}{\partial g}\Delta g + \frac{\partial c}{\partial r}\Delta r. \quad (1)$$

Here Δc is the relative uncertainty of the classification method. The derivative terms are the uncertainties in the classification method due to various parameters and are tabulated in Table 3; ΔT, Δdp, ΔAR, Δg, and Δr are the relative uncertainties in cloud-top temperature, depolarization, aspect ratio, asymmetry factor and effective radius, respectively. The overall uncertainty is computed on the basis of Eq. (1) and is listed in Table 4 for each habit. As expected, columns and plates have the lowest uncertainty of 9.7% and 11.3%, respectively. These habits are the most distinct and would have higher confidence classifications than other habits. Rosettes have the next lowest uncertainty with 20.1%. Fully developed rosettes will be easily distinguished from other habits, while budding rosettes are more likely to be misclassified. The irregular habits have higher uncertainties (29.4%, 45.4%, and 23.2%), as expected. Those groups contain fewer distinctions to separate them from others and likely contain a mix of asymmetric, nonpristine crystals. Spheroids have an uncertainty of 44.1% likely due to their small size which makes them difficult to distinguish from other groups. Spheroids have the smallest mean effective radius of all plate-like categories (30.57 μm). Additionally, spheroids likely contain a mix of irregularly shaped crystals, quasi-spherical droxtals, and even hexagonals as noted in the recent work of Lawson et al. (2019). Visual inspection of spheroids classified by CPI noted in Lawson et al. (2019) suggests that a significant fraction of spheroids may be small budding rosettes which adds to their uncertainty. Relative layer-integrated depolarization ratio uncertainties from CPL are reported as <10% (Yorks et al. 2011) while van Diedenhoven et al. (2012a, 2016a) report RSP relative uncertainties for aspect ratio (20%), effective radius (15%) and asymmetry factor (5%). Overall, the uncertainties presented are reasonable given the high-quality aircraft data used in the analysis. For potential space-based applications of this classification method, higher uncertainties would be expected.

6. Conclusions

By combining CPL and RSP cirrus cloud observations during the SEAC^{4}RS campaign, a *K*-means clustering technique was applied to classify optically thick cloud-top ice crystals into seven habit types. This technique demonstrates a finer classification than what is possible from lidar or polarimeter alone. It was determined that the most critical parameters for determining habit type are aspect ratio and cloud temperature, followed by depolarization ratio, asymmetry factor and effective radius. The results of this classification were compared to in situ CPI data and frequencies for irregulars, spheroids, columns and rosettes agreed within 5%, while less agreement was found for plates

TABLE 4. Overall uncertainties calculated for each crystal habit type with lowest uncertainty for distinct habits (plates, columns, and rosettes) and greater uncertainty for irregular crystals.

	Plates	Large plate-like irregulars	Small plate-like irregulars	Spheroids	Columns	Column-like irregulars	Rosettes
Overall uncertainty	11.3%	29.4%	45.4%	44.1%	9.7%	23.2%	20.1%

(~16%). The relationship between depolarization ratio and aspect ratio modeled by Noel et al. (2004) was successfully recreated using the combined CPL–RSP retrievals. Previous research showed a classification of ice crystals into three broad categories that were based on depolarization ratio, whereas the present classification can be expanded to seven categories. In addition, the high frequency of irregulars and spheroids in contrast to the relatively low number of observations of rosettes agrees well with the findings presented in Lawson et al. (2010) for similar anvil cirrus. These findings are expected to agree with those of Lawson et al. (2010) because in both studies, mostly fresh anvil still attached to convection were analyzed.

While radiative forcing models currently assume an oversimplified crystal classification of plates and columns, this unique dataset provides insights of ice crystal parameters for more detailed habit types. For the first time, lidar and polarimeter data are combined to provide valuable insight of microphysical ice crystal properties useful for model simulations and the ongoing investigation of radiative impacts of cirrus. Although depolarization ratio can be used for coarse habit classification, additional parameters such as aspect ratio and asymmetry factor provide information that is necessary for a finer classification.

The presented technique may be applied to combined measurements of the CALIOP lidar and POLDER instrument (van Diedenhoven et al. 2014), which were both in NASA's A-Train constellation. Combined backscatter lidar and a multichannel/polarization imager flown on board the same platform serves as a direct response to priorities set forth by NASA's Decadal Strategy for Earth Observation from Space (NASA 2018). The Aerosols, Clouds, Convection, and Precipitation (A-CCP) spaceborne mission also calls for combined lidar and polarimeter observations to study cloud and aerosol properties. The usefulness of a combined retrieval method is extensive; however, there is a dearth of coincident flights available for this kind of analysis. Additional coincident observations from lidar, polarimeter, and in situ instrumentation are necessary for finer habit classifications and parameterizations in radiative forcing models and to improve the technique of habit classification using remote sensing data that is shown here.

Acknowledgments. We acknowledge the support of NASA Grant 80 NSSC18K0887. Author B. van Diedenhoven is supported by NNX15AD44G. Author J. Zhang also acknowledges the support from NASA Grant NNX17AG52G and the Office of Naval Research Grant N00014-16-1-2040. Special thanks are given to the RSP team (principal investigator: Brian Cairns—NASA GISS) and SPEC, Inc., team (Paul Lawson) for their help with the RSP and CPI data.

REFERENCES

Alexandrov, M. D., B. Cairns, C. Emde, A. S. Ackerman, and B. van Diedenhoven, 2012: Accuracy assessments of cloud droplet size retrievals from polarized reflectance measurements by the research scanning polarimeter. *Remote Sens. Environ.*, **125**, 92–111, https://doi.org/10.1016/j.rse.2012.07.012.

Bailey, M., and J. Hallett, 2002: Nucleation effects on the habit of vapour grown ice crystals from −18° to −42°C. *Quart. J. Roy. Meteor. Soc.*, **128**, 1461–1483, https://doi.org/10.1002/QJ.200212858304.

——, and ——, 2004: Growth rates and habits of ice crystals between −20° and −70°C. *J. Atmos. Sci.*, **61**, 514–544, https://doi.org/10.1175/1520-0469(2004)061<0514:GRAHOI>2.0.CO;2.

——, and ——, 2009: A comprehensive habit diagram for atmospheric ice crystals: Confirmation from the laboratory, AIRS II, and other field studies. *J. Atmos. Sci.*, **66**, 2888–2899, https://doi.org/10.1175/2009JAS2883.1.

Baker, B. A., and R. Lawson, 2006: In situ observations of the microphysical properties of wave, cirrus, and anvil clouds. Part I: Wave clouds. *J. Atmos. Sci.*, **63**, 3160–3185, https://doi.org/10.1175/JAS3802.1.

Baran, A. J., P. N. Francis, S. Havemann, and P. Yang, 2001: A study of the absorption and extinction properties of hexagonal ice columns and plates in random and preferred orientations using exact T-matrix theory and aircraft observations of cirrus. *J. Quant. Spectrosc. Radiat. Transfer*, **70**, 505–518, https://doi.org/10.1016/S0022-4073(01)00025-5.

Bentley, W. A., and W. J. Humphreys, 1931: *Snow Crystals*. McGraw-Hill, 226 pp.

Cairns, B., E. E. Russell, J. D. LaVeigne, and P. M. W. Tennant, 2003: Research scanning polarimeter and airborne usage for remote sensing of aerosols. *Proc. SPIE*, **5158**, 33–44, https://doi.org/10.1117/12.518320.

Campbell, J. R., M. A. Vaughan, M. Oo, R. E. Holz, J. R. Lewis, and E. J. Welton, 2015: Distinguishing cirrus cloud presence in autonomous lidar measurements. *Atmos. Meas. Tech.*, **8**, 435–449, https://doi.org/10.5194/amt-8-435-2015.

Chepfer, H., P. Goloub, J. Riedi, J. F. de Haan, and J. W. Hovenier, 2001: Ice crystal shapes in cirrus clouds derived from POLDER-1/ADEOS-1. *J. Geophys. Res.*, **106**, 7955–7966, https://doi.org/10.1029/2000JD900285.

Comstock, J. M., T. P. Ackerman, and G. G. Mace, 2002: Ground-based lidar and radar remote sensing of tropical cirrus clouds at Nauru Island: Cloud statistics and radiative impacts. *J. Geophys. Res.*, **107**, 4714, https://doi.org/10.1029/2002JD002203.

Gan, G., C. Ma, and J. Wu, 2007: *Data Clustering: Theory, Algorithms, and Applications*. ASA-SIAM Series on Statistics and Applied Probability, SIAM, 466 pp.

Hioki, S., P. Yang, B. A. Baum, S. Platnick, K. G. Meyer, M. D. King, and J. Riedi, 2016: Degree of ice particle surface roughness inferred from polarimetric observations. *Atmos. Chem. Phys.*, **16**, 7545–7558, https://doi.org/10.5194/acp-16-7545-2016.

Holz, R. E., and Coauthors, 2016: Resolving ice cloud optical thickness biases between CALIOP and MODIS using infrared

retrievals. *Atmos. Chem. Phys.*, **16**, 5075–5090, https://doi.org/10.5194/acp-16-5075-2016.

Hong, G., and P. Minnis, 2015: Effects of spherical inclusions on scattering properties of small ice cloud particles. *J. Geophys. Res. Atmos.*, **120**, 2951–2969, https://doi.org/10.1002/2014JD022494.

Lawson, R. P., B. A. Baker, C. G. Schmitt, and T. L. Jensen, 2001: An overview of microphysical properties of Arctic clouds observed in May and July during FIRE ACE. *J. Geophys. Res.*, **106**, 14 989–15 014, https://doi.org/10.1029/2000JD900789.

——, ——, P. Zmarzly, D. O'Connor, Q. Mo, J.-F. Gayet, and V. Shcherbakov, 2006a: Microphysical and optical properties of atmospheric ice crystals at South Pole Station. *J. Appl. Meteor. Climatol.*, **45**, 1505–1524, https://doi.org/10.1175/JAM2421.1.

——, ——, B. Pilson, and Q. Mo, 2006b: In situ observations of the microphysical properties of wave, cirrus, and anvil clouds. Part II: Cirrus clouds. *J. Atmos. Sci.*, **63**, 3186–3203, http://doi.org/10.1175/JAS3803.1.

——, E. J. Jensen, D. L. Mitchell, B. Baker, Q. Mo, and B. Pilson, 2010: Microphysical and radiative properties of tropical clouds investigated in TC4 and NAMMA. *J. Geophys. Res.*, **115**, D00J08, https://doi.org/10.1029/2009JD013017.

——, and Coauthors, 2019: A review of ice particle shapes in cirrus formed in situ and in anvils. *J. Geophys. Res. Atmos.*, **124**, 10 049–10 090, https://doi.org/10.1029/2018JD030122.

Liou, K. N., Q. Cai, P. W. Barber, and S. C. Hill, 1983: Scattering phase matrix comparison for randomly hexagonal cylinders and spheroids. *Appl. Opt.*, **22**, 1684–1687, https://doi.org/10.1364/AO.22.001684.

Liu, C., R. L. Panetta, and P. Yang, 2014: The effective equivalence of geometric irregularity and surface roughness in determining particle single-scattering properties. *Opt. Express*, **22**, 23 620–23 627, https://doi.org/10.1364/OE.22.023620.

Mace, G. G., Q. Zhang, M. Vaughan, R. Marchand, G. Stephens, C. Trepte, and D. Winker, 2009: A description of hydrometer layer occurrence statistics derived from the first year of merged *Cloudsat* and *CALIPSO* data. *J. Geophys. Res.*, **114**, D00A26, https://doi.org/10.1029/2007JD009755.

Macke, A., J. Mueller, and E. Raschke, 1996: Single scattering properties of atmospheric ice crystals. *J. Atmos. Sci.*, **53**, 2813–2825, https://doi.org/10.1175/1520-0469(1996)053<2813:SSPOAI>2.0.CO;2.

McGill, M. J., D. L. Hlavka, W. D. Hart, V. S. Scott, J. D. Spinhirne, and B. Schmid, 2002: The Cloud Physics Lidar: Instrument description and initial measurement results. *Appl. Opt.*, **41**, 3725–3734, https://doi.org/10.1364/AO.41.003725.

——, ——, ——, E. J. Welton, and J. R. Campbell, 2003: Airborne lidar measurements of aerosol optical properties during SAFARI-2000. *J. Geophys. Res.*, **108**, 8493, https://doi.org/10.1029/2002JD002370.

——, M. A. Vaughan, C. R. Trepte, W. D. Hart, D. L. Hlavka, D. M. Winker, and R. Kuehn, 2007: Airborne validation of spatial properties measured by the CALIPSO lidar. *J. Geophys. Res.*, **112**, D20201, https://doi.org/10.1029/2007JD008768.

NASA, 2018: Decadal survey. NASA, https://science.nasa.gov/earth-science/decadal-surveys.

Neshyba, S. P., B. Lowen, M. Benning, A. Lawson, and P. M. Rowe, 2013: Roughness metrics of prismatic facets of ice. *J. Geophys. Res. Atmos.*, **118**, 3309–3318, https://doi.org/10.1002/JGRD.50357.

Noel, V., D. M. Winker, M. McGill, and P. Lawson, 2004: Classification of particle shapes from lidar depolarization ratio in convective ice clouds compared to in situ observations during CRYSTAL-FACE. *J. Geophys. Res.*, **109**, D24213, https://doi.org/10.1029/2004JD004883.

Sinclair, K., B. van Diedenhoven, B. Cairns, J. Yorks, A. Wasilewski, and M. McGill, 2017: Remote sensing of multiple cloud layer heights using multi-angular measurements. *Atmos. Meas. Tech.*, **10**, 2361–2375, https://doi.org/10.5194/amt-10-2361-2017.

Singh, A., A. Yadav, and A. Rana, 2013: *K*-means with three different distance metrics. *Int. J. Comput. Appl.*, **67**, 13–17, https://doi.org/10.5120/11430-6785.

Toon, O. B., and Coauthors, 2016: Planning, implementation and scientific goals of the Studies of Emissions and Atmospheric Composition, Clouds and Climate Coupling by Regional Surveys (SEAC^{4}RS) field mission. *J. Geophys. Res. Atmos.*, **121**, 4967–5009, https://doi.org/10.1002/2015JD024297.

Um, J., G. M. McFarquhar, Y. P. Hong, S.-S. Lee, C. H. Jung, R. P. Lawson, and Q. Mo, 2015: Dimensions and aspect ratios of natural ice crystals. *Atmos. Chem. Phys.*, **15**, 3933–3956, https://doi.org/10.5194/acp-15-3933-2015.

van Diedenhoven, B., 2018: Remote sensing of crystal shapes in ice clouds. *Light Scattering, Radiative Transfer and Remote Sensing*, A. Kokhanovsky, Ed., Springer, 197–250.

——, A. M. Fridlind, A. S. Ackerman, and B. Cairns, 2012a: Evaluation of hydrometeor phase and ice properties in cloud-resolving model simulations of tropical deep convection using radiance and polarization measurements. *J. Atmos. Sci.*, **69**, 3290–3314, https://doi.org/10.1175/JAS-D-11-0314.1.

——, B. Cairns, I. V. Geogdzhayev, A. M. Fridlind, A. S. Ackerman, P. Yang, and B. A. Baum, 2012b: Remote sensing of ice crystal asymmetry parameter using multi-directional polarization measurements—Part 1: Methodology and evaluation with simulated measurements. *Atmos. Meas. Tech.*, **5**, 2361–2374, https://doi.org/10.5194/amt-5-2361-2012.

——, ——, A. M. Fridlind, A. S. Ackerman, and T. J. Garrett, 2013: Remote sensing of ice crystal asymmetry parameter using multi-directional polarization measurements—Part 2: Application to the Research Scanning Polarimeter. *Atmos. Chem. Phys.*, **13**, 3185–3203, https://doi.org/10.5194/acp-13-3185-2013.

——, A. M. Fridlind, B. Cairns, and A. S. Ackerman, 2014: Variation of ice crystal size, shape and asymmetry parameter in tops of tropical deep convective clouds. *J. Geophys. Res. Atmos.*, **119**, 11 809–11 825, https://doi.org/10.1002/2014JD022385.

——, ——, ——, ——, and J. Yorks, 2016a: Vertical variation of ice particle size in convective cloud tops. *Geophys. Res. Lett.*, **43**, 4586–4593, https://doi.org/10.1002/2016GL068548.

——, A. S. Ackerman, A. M. Fridlind, and B. Cairns, 2016b: On averaging aspect ratios and distortion parameters over ice crystal population ensembles for estimating effective scattering asymmetry parameters. *J. Atmos. Sci.*, **73**, 775–787, https://doi.org/10.1175/JAS-D-15-0150.1.

Wendisch, M., and Coauthors, 2005: Impact of cirrus crystal shape on solar spectral irradiance: A case study for subtropical cirrus. *J. Geophys. Res.*, **110**, D03202, https://doi.org/10.1029/2004JD005294.

Wylie, D. P., and W. P. Menzel, 1999: Eight years of global high cloud statistics using HIRS. *J. Climate*, **12**, 170–184, https://doi.org/10.1175/1520-0442(1999)012<0170:EYOHCS>2.0.CO;2.

Yorks, J. E., D. L. Hlavka, W. D. Hart, and M. J. McGill, 2011: Statistics of cloud optical properties from airborne lidar measurements. *J. Atmos. Oceanic Technol.*, **28**, 869–883, https://doi.org/10.1175/2011JTECHA1507.1.

Zhang, Y., A. Macke, and F. Albers, 1999: Effect of crystal size spectrum and crystal shape on stratiform cirrus radiative forcing. *J. Atmos. Res.*, **52**, 59–75, https://doi.org/10.1016/S0169-8095(99)00026-5.